Facultad de Ciencias

Robot software for the assembly of modules of the Endcap Timing Layer of the CMS detector

(Software de robot para el ensamblado de módulos del Endcap Timing Layer del detector CMS)

Trabajo de Fin de Grado para acceder al

Grado en Física

Author: Víctor Calzada Cabano

Director: Pablo Martinez Ruiz del Árbol

September - 2020

Acknowledgments

To my supervisor , Dr.Pablo Martinez Ruiz del Arbol, for his guidance and his patience throughout this project. To my teachers, for the invaluable knowledge they have provided me this last 4 years. Finally to my family and friends for their support and understanding on this journey.

Abstract

This project is centered on the programming and utilization of ACE's software in order to obtain a deeper and richer understanding of the V+ programming language. Access to this tools will be essential in order to build the electronic components needed for the new modules of the Endcap Timing Layer (ETL), one of the new additions to the CMS' experiment on the upcoming upgrade.

The amortization of the assembly process is essential due to the large amount of needed modules, roughly 9000.

Resumen

Este proyecto se centra en la programación y utilización de software ACE con el fin de obtener un entendimiento mas profundo y rico del lenguaje de programación V+. El acceso a estas herramientas será esencial para la construcción de los circuitos electrónicos pertenecientes a los nuevos módulos del Endcap Timing Layer (ETL), una de las nuevas introducciones al detector CMS en el próximo upgrade.

La automatización en el proceso de montado es esencial debido la enorme cantidad de modulos requeridos, rondando los 9000.

Contents

Chapter 1

Introduction

This project frames in the context of instrumentation for Particle Physics detectors, being the ultimate goal to ensure a better understanding of the universe and the fundamental interactions that take place in it. The final outcome will be the enrichment of our knowledge on the branch of physics called particle physics.

1.1 Particle physics

Particle physics is at the core of our understanding of the universe. Our knowledge on this field has been acquired through decades of theoretical developments and experiments condensed on the so-called Standard Model (SM) of Particle Physics. The Standard Model (SM) is one of the greatest achievements of modern physics due to it's successful description of all current experimental data.

Our knowledge on the building blocks of the Universe has varied along the years depending on the accessible energy scales. At low energies, matter seems to be formed by atoms, which are the bound state of positively charged protons (p), neutral electrically charged neutrons (n) and negatively charged electrons (e^-). This simplistic picture of the world rapidly changes at higher energy scales where further structure is observed, Figure 1.1.

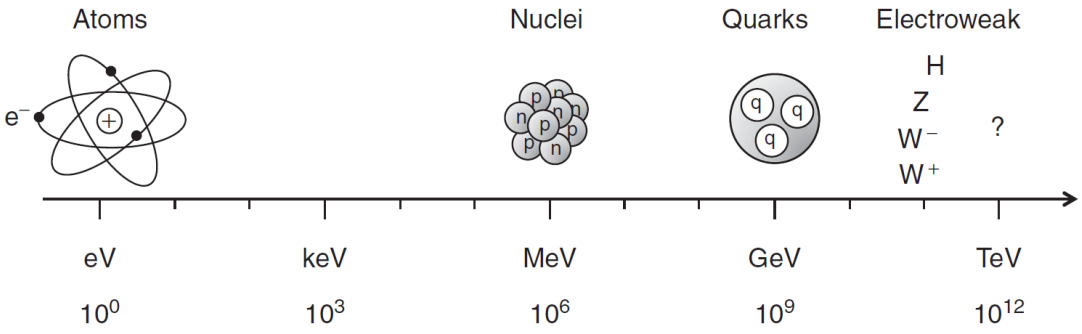

Figure 1.1: Complexity of the universe at different energy scales, from eV to TeV [1].

While even at higher energies the electron doesn't show further structure, the proton and the neutron do. Protons and neutrons are bound states of quarks which are believed to be fundamental and therefore indivisible particles. Both neutrons and protons are bound states of two quarks, the proton consist of two up-quarks and one down-quark while the neutron consists of two down-quarks and one up-quark. These two quarks, up-quark (u) and down-quark (d), the electron (e^-) and the nearly massless electron neutrino (ν_e) form the first generation of particles described by the Standard Model. As mentioned before, higher energy reveals further complexity having the Standard Model a second and a third generation of particles only encountered in high-energy particle colliders. The charm-quark (c), strange-quark (s), the muon (μ^-) and the muon neutrino (ν_μ) constitute the second generation of particles and finally the top-quark (t), bottom-quark (b), the tau (τ^-) and the tau neutrino (ν_τ) form the third generation of particles. A particle from one generation shares the same fundamental qualities as one particle from the other two generations, being the only difference their mass, Figure 1.2, which increases with each generation, therefor accounting for the increase of energy on their discovery. All the particles from the 3 generations have half odd integer spin, therefore they are categorized as fermions.

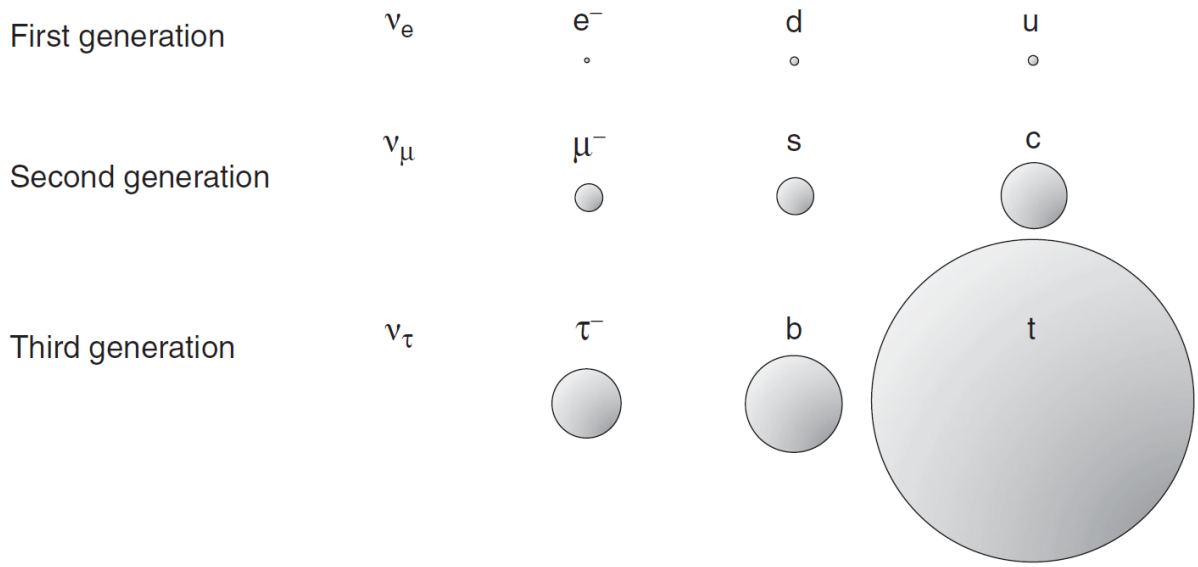

Figure 1.2: Three generations of fundamental particles whit the representation of their masses indicated by their size [1].

Neutrinos are not represented on Figure 1.2 indicating that their masses, even if not zero, are very small compared to the other particles. Indeed, their masses are so small that its determination has been impossible to date and its established upper limit suggest that they are at least nine orders of magnitude lighter than the other fermions.

Particle physics is also in charge of the study of the fundamental forces, gravity, electromagnetism, the strong force and the weak force which are the mechanism the fun-

damental particles interact with each other. While gravity plays a fundamental roll on a macroscopic scale, the gravitational force between two individual particles is too small to take in consideration against the other three fundamental interactions. The weak interaction directly affects all twelve fundamental particles while all but the three neutrinos, which are not electrically charged, participate in the electromagnetic interaction. Finally, only the quarks feel the strong force, resulting in different properties from the electron, muon, tau and their neutrinos, which are referred within the SM as leptons.

			strong	electromagnetic	weak
Quarks	down-type up-type	d s b u c t	yes	yes	yes
Leptons	charged neutral	e^- μ^- τ^- ν_e ν_μ ν_τ	no	yes no	yes

Table 1.1: Quarks and leptons and the different interactions the experience.

The 3 fundamental interactions, all except gravity, are described by Quantum Field Theory (QFT) therefore eliminating the classical problem of action-at-a-distance. Description of the forces between two particles in QFT calls for for the existence of a virtual particle exchanged by the two interacting particles. Virtual particles have the roll of mediating the interaction which is achieved by transferring momentum from one particle to the other. As an example, focusing on electromagnetism we find the theory of Quantum Electro-dynamics (QED) in charge of explaining the interactions between charged particles like electrons. In the case of two electrons, one possible interaction is as shown on Figure 1.3, an scattering, in which the upper electron emits a photon then absorbed by the lower electron thus successfully transferring momentum from one electron to the other, which is manifested as the electromagnetic force. Time on both diagrams in Figure 1.3 runs from left to right, therefore, the second diagram showcase the other possible time-ordering of the scattering.
In the same manner as in QED, the strong and weak force are described by the exchange of a spin-1 force-carrying particle, known as a gauge boson. The boson associated with the strong interaction is known as the gluon and the mediators for the weak-charged current are the W^+ and W^-. The weak interaction has another mediator for the weak-neutral current, the Z boson. Whilst the photon and the gluon, mediators for the electromagnetic and strong interaction, are massless, the mediators for the weak interaction are not, having that the masses of the W^+ and W^- are approximately eight times more massive than the proton.

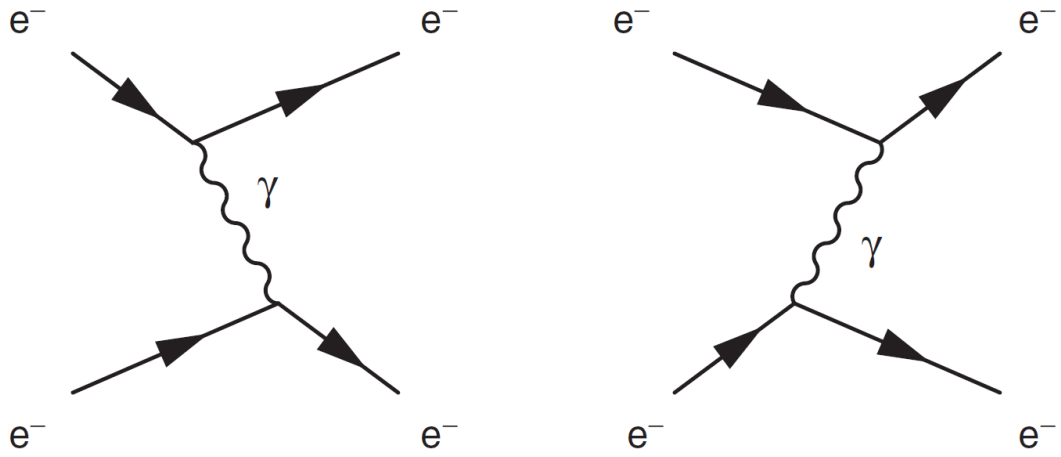

Figure 1.3: Scattering of two electrons by the exchange of a photon. Diagram includes two possible time-orderings [1].

The interactions given by the fundamental forces, are experimentally observable phenomena which can be described as the transition between different quantum mechanical states. The transition rate Γ_{fi} is the probability of a transition per unit time from an initial state $|i\rangle$ to a final state $|f\rangle$, and in non-relativistic quantum mechanics is given by the Fermi's golden rule

$$\Gamma_{fi} = 2\pi |T_{fi}|^2 \phi(E_i) \tag{1.1}$$

where $\phi(E_i)$ is the density of states and T_{fi} is the transition matrix element. As we can see the transition rate has a dependency on 2 components: the transition matrix element, which is in charge of reflecting the fundamental particle physics; the density of accessible states, which depends on the kinematics of the process. The transition matrix element is given by the Hamiltonian for the interaction and is given by the perturbation expansion

$$T_{fi} = \langle f|V|i\rangle + \sum_{j \neq i} \frac{\langle f|V|j\rangle\langle j|V|i\rangle}{E_i - E_j} + ... \tag{1.2}$$

This first terms in the perturbation series can be interpreted as scattering in a potential V and scattering via and intermediate state j as shown in Figure 1.4.

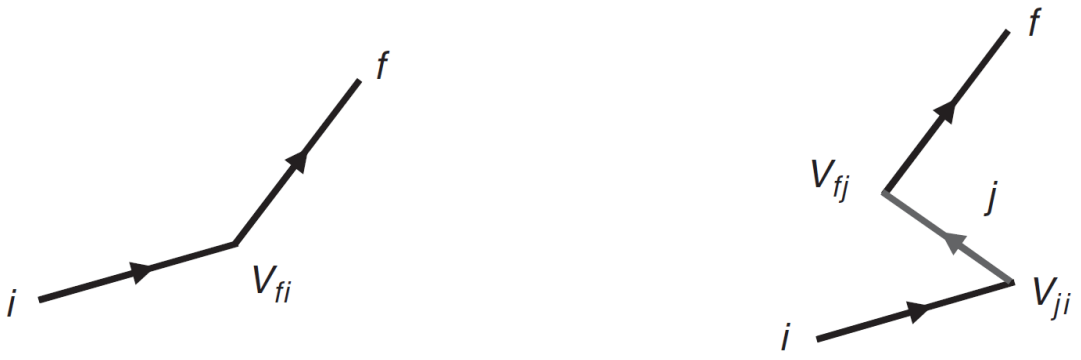

Figure 1.4: Scattering: in an external potential, via an intermediate state j [1].

This accounts for the transfer of momentum in any interaction. An scattering in a potential results in a transfer of momentum without a mediating body, but as indicated in Figure 1.4 interactions are mediated by the exchange of particles eliminating the mysterious action at a distance. This indicates that the forces are merely a result from the transfer of momentum.

Other important concept of particle physics concerning the interaction of particles is the cross section. A flux of particles is the number of particles that cross a unit area per unit time. Having a beam of particles a, with flux ϕ_a, which are crossing a region of space where particles b are present, the interaction rate r_b between this 2 particles can be written:

$$r_b = \sigma\phi_a \tag{1.3}$$

where we find the interaction cross section σ, which has dimensions of area. There are situation where the cross section is indeed closely related with physical cross sectional area of the particle target. However, the cross section represents the quantum mechanical probability of an interaction

As mentioned before, the mediators for the electromagnetic and strong interaction are massless, but we find that the two forces are vastly different. Whilst Quantum Electrodynamics correspond to a U(1) local gauge symmetry of the Universe, the underlying symmetry associated with Quantum Chromodynamics (QCD), Quantum Field Theory that explains the strong interaction, is invariance under SU(3) local phase transformations. From this different symmetry arise qualities only associated with the strong interaction. First consequence of this behaviour of QCD is the introduction of a new degree of freedom known as colour with red, blue and green labelling the states [1]. It becomes necessary the introduction of eight new fields which correspond with the generators of the SU(3) symmetry, this eight fields are the eight gluons of QCD in contrast with QED that only has one photon. Finally, from the transformation of the new fields arise an additional term which gives the gluons self-interaction and therefor colour charge, Figure 1.5.

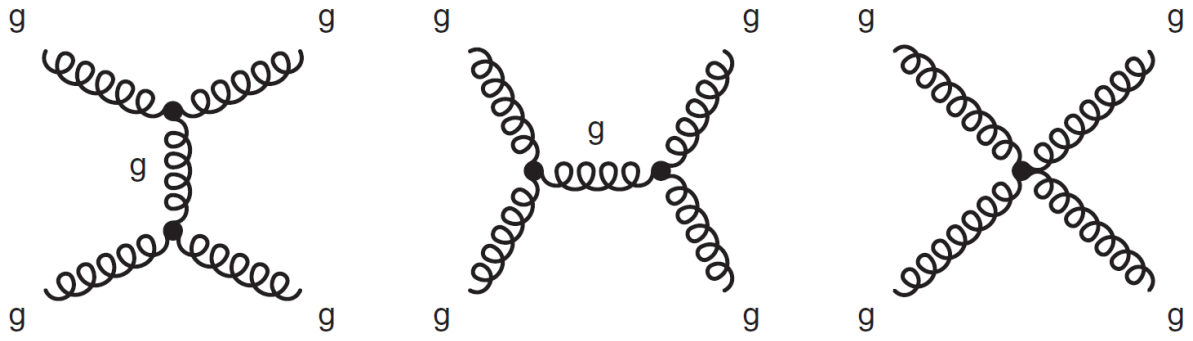

Figure 1.5: Gluon-gluon interacting process. Lowest-order Feynman diagrams, triple and quartic gluon vertices [1].

The strong interaction is also responsible for the non existence of free quarks, which

is explained by the colour confinement. Color confinement is a direct consecuence of gluon-gluon self-interaction, therefore, only particles with zero color charge are able to propagate freely. When two quarks are pulled apart there is an attractive interaction thus an exchange of virtual gluons, Figure 1.6a. This gluons, which posses color charge, now interact with each other resulting on the field lines between the two quarks squeezing into a tube, Figure 1.6b. When the two quarks are sufficiently apart the energy contained in the tube is constant, being the energy proportional to the separation of the quarks. As the distance between the quarks increases the energy does as well, therefore it would be necessary and infinite amount of energy to separate two quarks to infinity [1]. Hence coloured particles gather into colourless combinations, explaining why quarks are always confined.

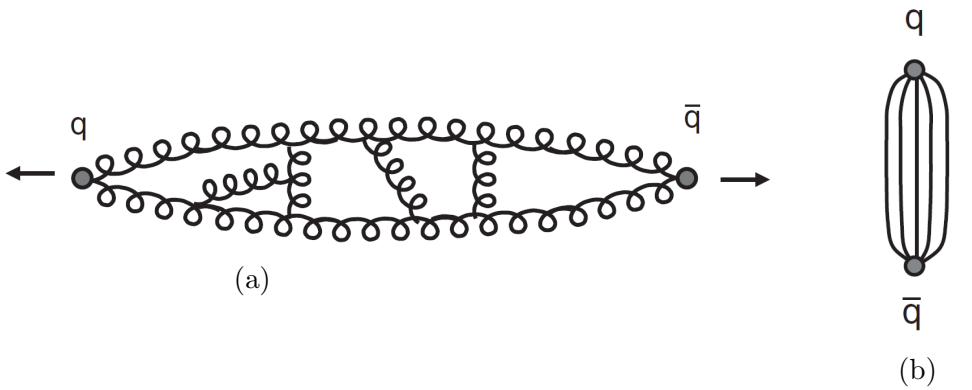

Figure 1.6: Gluon-gluon interaction on long-range QCD interaction [1].

A direct consecuence of the colour confinement is the detection of jets on the study of high-energy particle collisions. The detection of jets is common in reactions such as $e^+ + e^- \rightarrow q + \bar{q}$, where high-energy electrons and positrons collide with equal opposite momenta, causing for the system composed of all hadrons produced to have zero momentum. An initial electromagnetic process leads to the production of a quark-antiquark pair and as consecuence of colour confinement this quarks are observed as jets of colourless particles [2].

The process of jets production is called hadronisation. The quark-antiquark produced on the collision depart at high velocities on opposites directions due to the conservation of momenta. As mentioned before, the energy density of the colour field increases as the particles drift apart from each other, as mentioned before. At a certain distance, there is enough energy to form new $q\bar{q}$ pairs. This process continues forming new $q\bar{q}$ pairs and finally, when the energy has decreased, all the quark combine to colourless hadrons, Figure 1.7 [1].

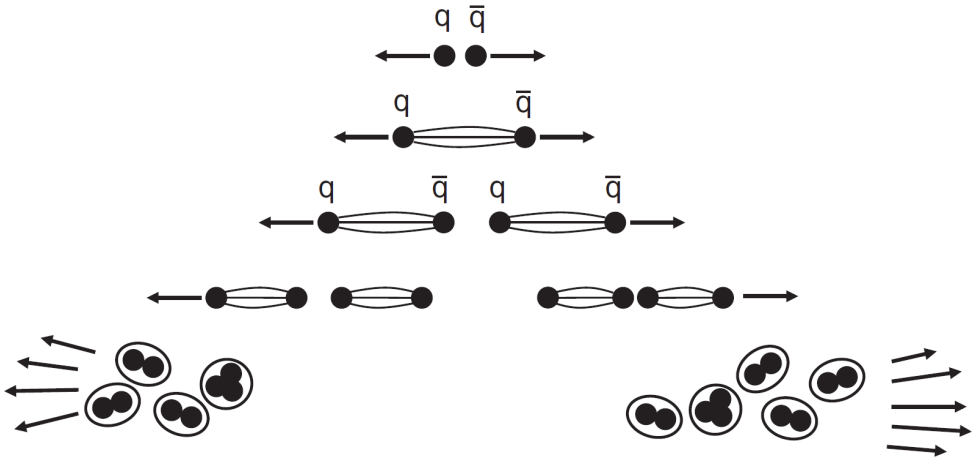

Figure 1.7: Hadronisation process [1].

The last force which depends on the exchange of a gauge boson, as described by the Standard Model, is the weak interaction, which follows the $SU(2)_L$ gauge symmetry. Within this interaction it can be made one differentiation between weak charged-current interaction and neutral-current interaction, depending on the boson that intervenes. Differences with the other interactions arise from the fact that its bosons have mass. One consecuence of the mass of this bosons is the limited range of the interaction, 10^{-18} m [3]. Another characteristic only encountered on the weak interaction is the violation of parity, first observed in 1957 when Wu and collaborators studied nuclear β-decay of polarised cobalt-60, ${}^{60}Co \rightarrow {}^{60} Ni^* + e^- + \bar{\nu}_e$ [1].

Completion of the Standard Model comes with the introduction of the Higgs field, the associated Higgs boson and the Higgs mechanism, and without this inclusions the Standard Model is not a consistent theory. From the the local gauge symmetries that govern the QED, QCD and weak interaction we obtain massless propagators of the interactions. This is not a problem for QED and QCD where indeed the gauge bosons are massless, but it enters in direct contradiction with the experimental data regarding the large masses of W and Z bosons. This phenomena are not restricted to the gauge bosons, facing similar problems with other particles of the Standard Model.

Despite the incredible success of the Standard Model, there is still holes in our knowledge. While the Standard Model is able to explain a bast portion of the physics that surround us, there are other possible theories for the nature of the universe, for example supersymmetry, large-scale extra dimensions, and string theory. Some questions still unanswered by the Standard Model are, for example the nature of dark matter, the unification of forces, the description of gravity as a gauge theory and many more.

In order to answer this questions, the Standard Model is taken to its limits in huge installations such as the LHC where particles at enormous energies collide and the result of this collisions are studied.

1.2 Large Hadron Collider (LHC)

Information gathered in this section and the following subsections summarise the content provided by [4, 5]. The Large Hadron Collider (LHC) is world's largest and most powerful particle accelerator. It is a two-ring-superconducting-hadron accelerator and a collider built in a 26.7 km tunnel originally constructed between 1984 and 1989 for the CERN Large Electron-Positron collider (LEP) machine. The construction of LHC at CERN was highly encouraged by the already existing tunnel used for the LEP and its injection chain. This decision carried some issues such as the fact that the LEP machine had eight crossing points flanked by long straight sections for radiofrequency cavities in order to compensate the synchrotron radiation losses. This kind of problem do not transfer to the LHC machine where idealy would have longer arcs and shorter straight sections for the same circumference [4]. The injection chain of LHC is as follows; Linac2 - Proton Synchrotron Booster (PSB) - Proton Synchrotron (PS) - Super Proton Synchrotron (SPS). A layout of the injection chain is shown in Figure 1.8.

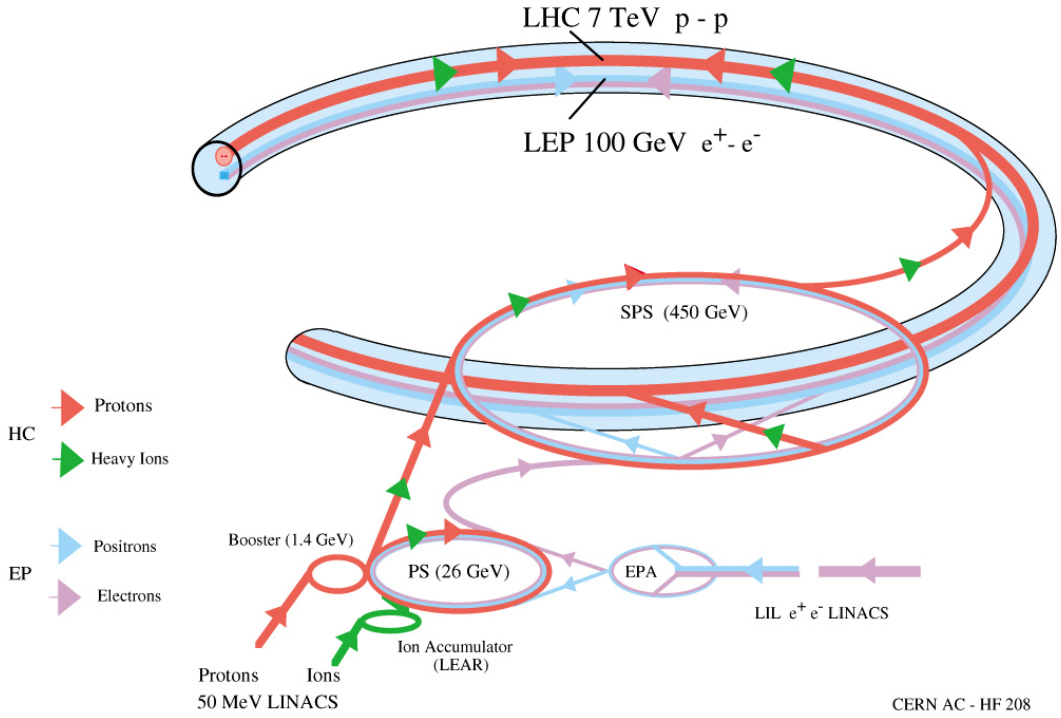

Figure 1.8: The LHC injection complex [6].

The main objective of the LHC is to test the Standard Model in order to unfold new physics beyond the knowledge we already posses. The center of mass collision energies is up to 14 TeV, with a number of events given by:

$$N_{event} = L\sigma_{event} \tag{1.4}$$

where σ_{event} corresponds to the cross section of the event and L is the machine luminosity, which only depends on the beam parameters:

$$L = \frac{N_b^2 n_b f_{rev} \gamma_r}{4\pi \epsilon_n \beta *} F \tag{1.5}$$

where N_b is the number of particles per bunch, n_b the number of bunches per beam, f_{rev} the revolution frequency, γ_r the relativistic gamma factor, ϵ_n the normalized transverse bean emittance, $\beta*$ the beta function at the collision point and F the geometric luminosity reduction factor due to the crossing angle at the interacting point. This equation allow as to write the beam as a Gaussian beam distribution.

The LHC counts with two high luminosity experiments, ATLAS (F. 1.9a) and CMS (F. 1.9b), reaching a peak luminosity of $L = 10^{34}$ cm^{-2} s^{-1} for proton operation. LHC also has two low luminosity experiments: LHC-B (F. 1.9c) for β-physics, with a peak luminosity of $L = 10^{32}$ cm^{-2} s^{-1}, and TOTEM for the detection of protons from elastic scattering at small angles, achieving a peak luminosity of $L = 2 \times 10^{29}$ cm^{-2} s^{-1}. It can also be found a dedicated ion experiment, ALICE (F. 1.9d), with a peak luminosity of $L = 10^{27}$ cm^{-2} s^{-1} for nominal lead-lead ion operation.

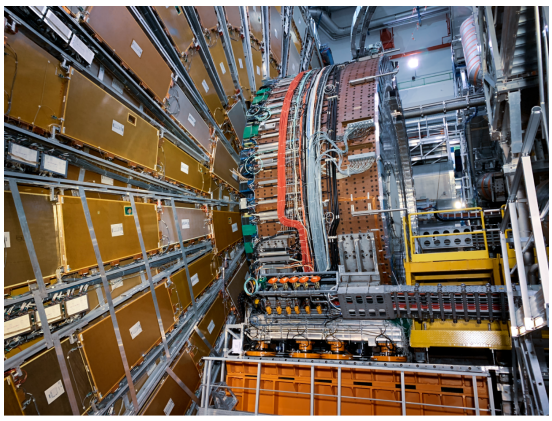

(a) ATLAS [7].

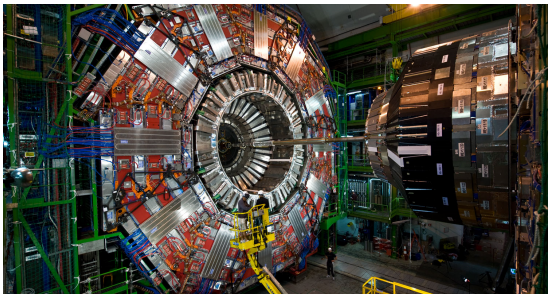

(b) CMS [8].

(c) LHC-B [9].

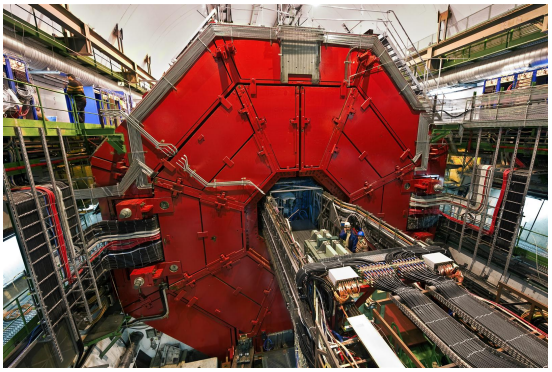

(d) ALICE [10].

Figure 1.9: Experiments at LHC

This work is framed in the context of the Compact Muon Detector (CMS), further explored on the following subsections.

1.2.1 Compact Muon Solenoid (CMS)

The Compact Muon Solenoid was build for the study of proton-proton collisions as well as lead-lead collisions. The parameters for both studies are different having a center-of-mass energy of 14 TeV and a luminosity of $L = 10^{34}$ cm^{-2} s^{-1} for the proton-proton collisions, and a center-of-mass energy of 5.5 TeV and a luminosity of $L = 10^{27}$ cm^{-2} s^{-1} for the lead-lead collisions. At the given luminosity the event rate at the detector is approximately of 10^9 events/s. In order to be stored and analysed, the online event selection process (trigger) must be able to reduce this quantity to 100 events/s.

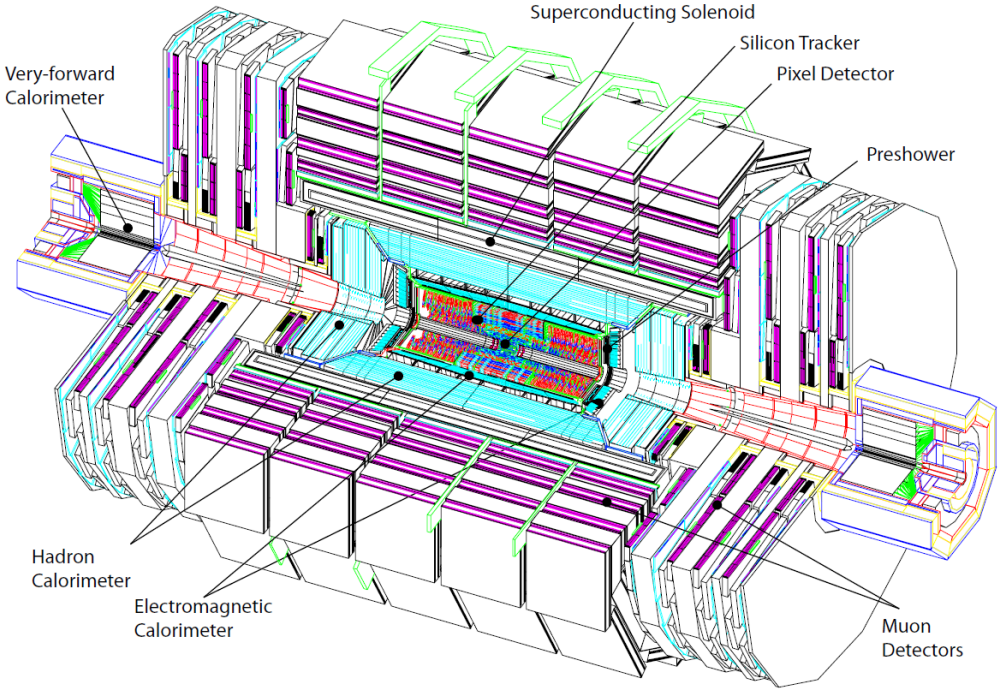

Figure 1.10: CMS layout

The detector dimensions are as follows: a length of 21.6 m, a diameter of 14.6m ad a total weight of 12500 t. The detector counts with a 13 m long, 6 m in diameter superconducting solenoid. Both the inner tracker and the calorimeter fit inside the massive solenoid while the muon detectors lie just outside the structure, Figure 1.10.

1.2.1.1 Superconducting magnet

The superconducting magnet with dimensions of 12.5 m in length and 6 m diameter was built to achieve a 4 T field. At full current it has a stored energy of 2.6 GJ. The flux is

able to return through a 10000 t yoke comprising 5 wheels and two endcaps of three disks each. The 220 t cold mass, part of the CMS solenoid designed to operate at liquid helium temperature, is the 4-layer loop made from a stabilised reinforced NbTi conductor. The magnet was originally assembled and tested on the surface and then lowered 90 m under ground to its final destination.

Grand part of the CMS coil must have a structural function. This is due to the shear stress level inside the winding which could cause cracking in the insulation. For this reason the structural material cannot be far from the current carrying elements, which is fixed by utilizing a self-supporting conductor, innovation design introduced on the CMS magnet.

1.2.1.2 Inner tracking system

The inner tracking system surrounds the interaction point, with 5.8 m of length and 2.5 m of diameter. The magnetic solenoid wraps up the tracking system and provides a homogeneous magnetic field of 4 T. Its main objective is to execute a precise and efficient measurement of the trajectories of charged particles and the reconstruction of secondary vertices. The biggest challenge for the construction of the inner tracking system was the selection of materials due to the extreme conditions and the requirements requested for the detector. The high precision both in the measurements and the reconstruction of the trajectories of the charge particles required a high granularity and a fast response. Both of this qualities for a detector lead to a high power density and therefore it is needed an efficient cooling system. However, this addition could lead to multiple scattering, bremsstrahlung, photon conversion or nuclear interaction which are to be avoided at all cost. The high luminosity and intense particle flux may cause sever radiation damage. These requirements lead to a tracked design based on silicon. The CMS tracker is composed of a pixel detector with three barrel layers and a silicon strip tracker with 10 barrel detector layers. Both systems are completed with the corresponding endcaps, 2 disks for the pixel detector and 3 plus 9 disks for the strip detector on each side. With 200 m^2 of area makes the CMS tracker the largest silicon detector ever built.

The pixel system is closest to the interaction region. CMS relies in its small impact paremeter resolution for a good secondary vertex reconstruction. Its position near the interacting zone allows for a precise tracking on z (along the interacting zone) and $r - \phi$ (along the circunference of the detector). The size of each pixel is $100 \times 150\ \mu m^2$ with the intention to obtain similar track resolution in both directions, z and $r - \phi$. The spatial resolution for the detector is in the range of 15-20 μm. The mechanism for the detector has been designed to allow a yearly access if needed, while at full luminosity it is expected to stay operational at least 2 years.

Each detector is based on the so called n-on-n concept. High dose n-implants introduced into a high resistance n-substrate. The rectifying pn-junction lies on the back side of the sensor surrounded by a multi guard ring structure. The selection pf the n-on-n

concept for this sensors allows for a high signal charge at moderate bias voltage (< 600 V).

For the strip detector it is found a p-on-n type silicon micro-strip sensor. An aluminium strip covers each detector and for it to be electrically insulated it is covered with a silicon oxide and a nitride multilayer. This allows for AC coupling of the signals which go from the strip to the electronics.

1.2.1.3 Electromagnetic calorimeter (ECAL)

The electromagnetic calorimeter (ECAL) has 61200 lead tungstate ($PbWO_4$) crystals placed on the central barrel and is closed by 7324 crystals in each of the two endcaps. In front of both endcaps it is found a preshower detector. Vacuum phototriodes (VPTs) are used as photodetectors on the endcaps while avalanche photodiodes (APDs) are used in the barrel. In order to achieve a fast response, fine granularity and radiation resistant it is used high density crystals.

The $PbWO_4$ crystals are a great choice for operation at LHC due to its high density (8.28 g/cm^3), short radiation length (0.98 cm) and small Molière radius (2.2 cm), which result in a fine granularity and a compact calorimeter. The crystal are polished after machining to achieve total internal reflection and therefore optimal light collection on the photodetector. Due to its truncated pyramidal shape, a fully polished crystal would make the light collection non-uniform along the crystal length. To achieve uniformity it is required to depolish one lateral face. This phenomena of non-uniformity is large because of the high refractive index (n = 2.29 around the peak wavelength). Light at the endcaps is naturally more uniform, which is caused by the parallel placement of the crystal faces. Barrel and endcap crystals are shown in Figure 1.11.

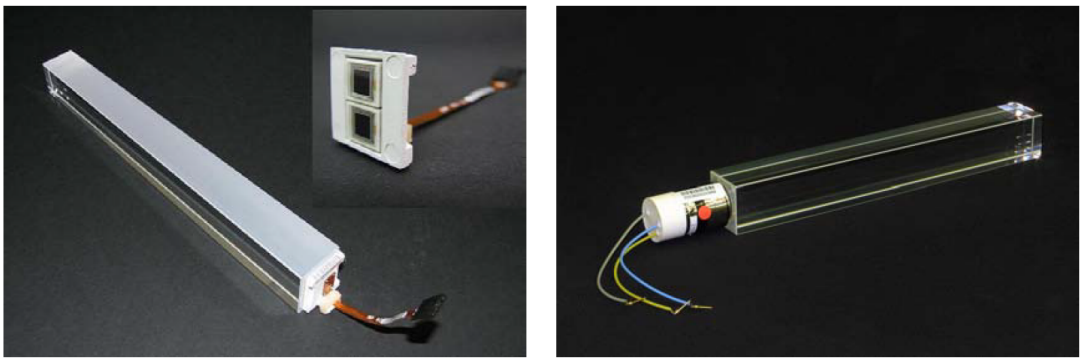

Figure 1.11: ECAL $PbWO_4$ crystals with photodetectors. Left figure: Barrel crystal with upper face depolished and the APD capsule. Right figure: Endcap crystal and VPT.

The barrel covers the pseudorapidity range $|\eta| < 1.479$. The shape of each crystal varies with the position in η. Avoiding cracks aligned with particle trajectories they are mounted in a quasi-projective geometry. The crystals are placed in a thin-walled alveolar

structure called submodule, which contains only a pair of shapes. The submodules are contained in to modules of different types, in relation with the position in η, each counting with 400 or 500 crystals. Modules are assembled in a supermodule, with 1700 crystals. The endcaps cover $1.479 < |\eta| < 3.0$. The endcaps count with identically shaped crystals arranged in mechanical units (supercrystals) consisting of carbon fiber alveola structure. The endcaps are divided into 2 halves called Dees, having each Dee 3662 crystals. The internal structure of the calorimeter is shown in Figure 1.12.

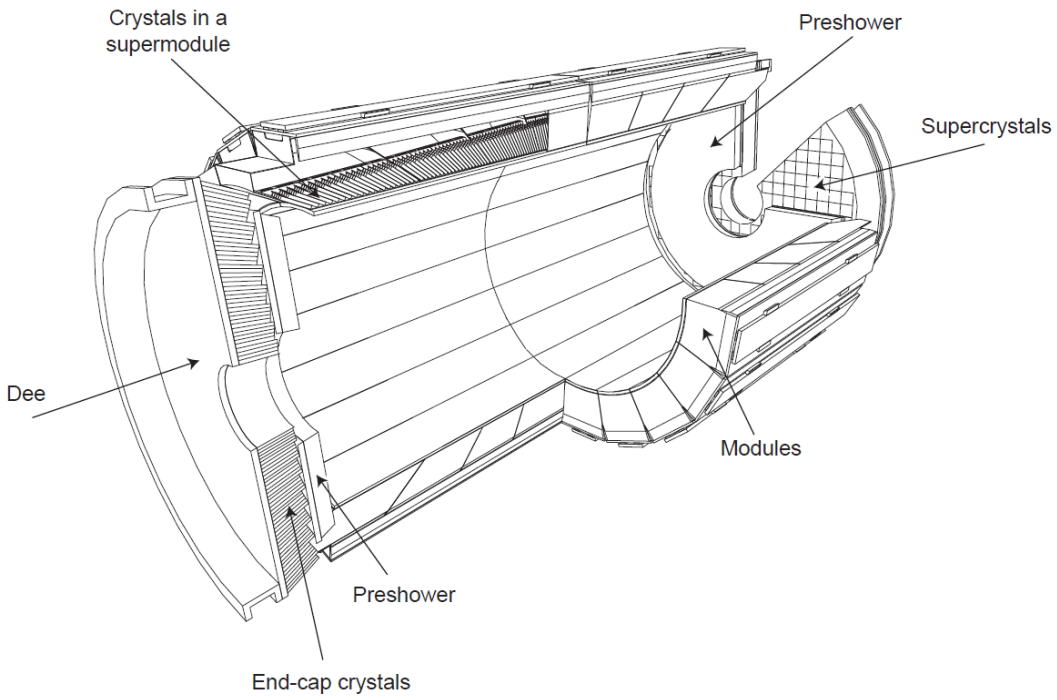

Figure 1.12: Internal arrangement of the crystals within the CMS electromagnetic calorimeter.

1.2.1.4 Hadron calorimeter (HCAL)

The hadron calorimeter (HCAL) importance lies in the measurement of hadron jets and neutrinos or exotic particles resulting in apparent missing transverse energy. The barrel covers a pseudorapidity range of $|\eta| < 1.3$ and its divided into 2 halves. It is formed of 36 azimuthal wedges or parts made out flat absorber plates parallel to the beam axis. For structural purpose the innermost and outermost plates are made of stainless steel. It also counts with scintillators arrange on 70000 tiles which are placed on layers.

The endcap covers the pseudorapidity $1.3 < |\eta| < 3.0$. It is required a high radiation tolerance and a non magnetic material since the calorimeter is inserted into the end of the 4 T magnet solenoid. As well as in the barrel, it is found absorber materials and scintillators in order to carry away its intended purpose.

1.2.1.5 Muon system

The muon system is an important structure for the recognition of signatures of interesting processes over the background at the LHC with full luminosity. One example is the detection of 4 muon, which decay from ZZ or ZZ* and this 2 pairs decay from the Standard Model Higgs boson. The muon system has 3 mayor roles: muon identification, momentum measurement and triggering. The measurement of the momentum and the triggering capabilities are possible due to the high field solenoidal magnet. It is used 3 types of gaseous particles detectors for muon identification.

The CMS barrel muon detector is formed out of 4 stations which form a concentric cylinder around the z axis. The 3 inner cylinders have 60 drift chambers and the outer cylinder has 70. The barrel covers a pseudorapidity of $|\eta| < 1.2$. The structural support for the detector consists in an iron yoke where it can be found 4 muon chambers per wheel, labeled MB1, MB2, MB3, and MB4. A layout of the barrel is shown in Figure 1.13.

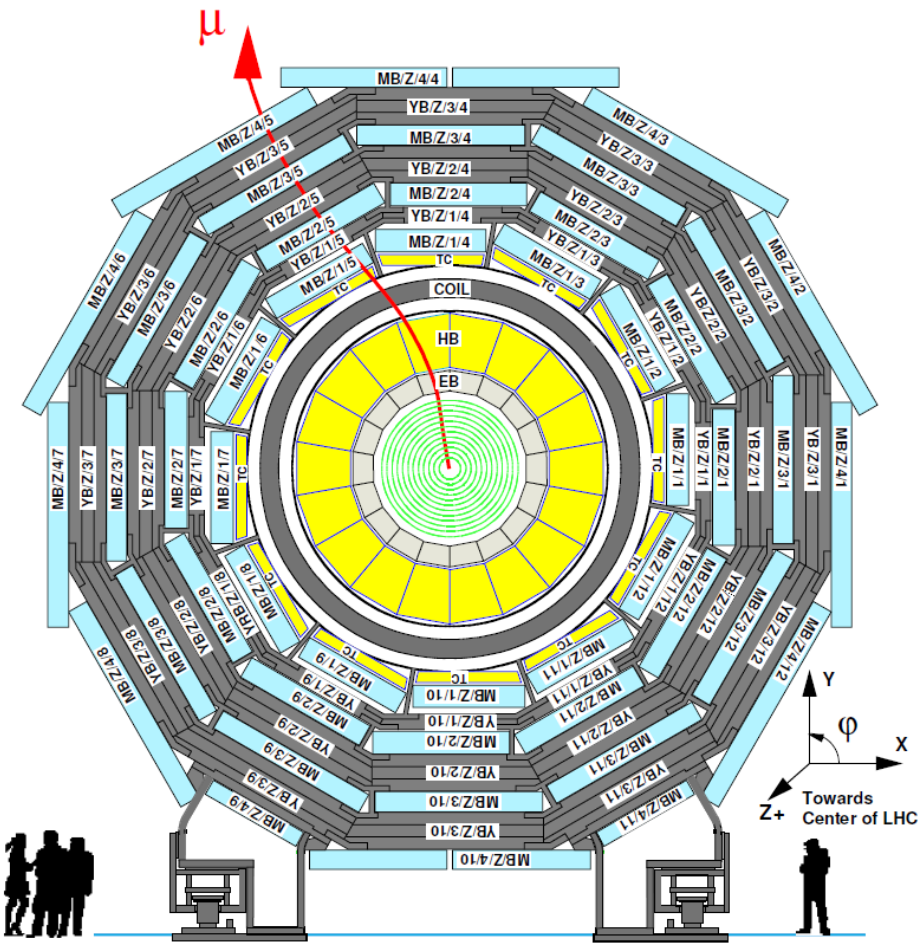

Figure 1.13: Layout of the CMS barrel muon detector.

1.3 High Luminosity Large Hadron Collider (HL-LHC)

In spite of the huge success that the LHC showed with the discovery of the Higgs boson, no signs of Physics Beyond the Standard Model have been found. Since then, the LHC has contributed to the understanding of the universe by eliminating theories and models, others have had their parameters sharply limited and in others refinement of their search strategies have been carried out in order to be more sensitive to hard-to-identify configurations. These points are being applied, for example, to the "stealth" SUSY (supersymetry), having the case that new particles look very similar to the SM background and to "compressed" SUSY, where there would be particles with very similar masses making some decay configurations very hard to observe. Sensitivity of CMS will improve with the increasing luminosity of the HL-LHC in order to observe SUSY and many other new physics signals. Sources used on this section and further documentation can be found in [11, 12].

Precision studies such as the study of the Higgs and the search for new physics require a high increase of the luminosity of LHC. The increase of luminosity demands for upgrades on the CMS detector so as to preserve the efficiency, resolution and background rejection at these high luminosities. Planning to increase the luminosity of the LHC carried out by CERN began before the machine went into operation. The current plan calls for a series of long periods of data-taking, referred to as Run-I, Run-II, etc. interleaved with long shutdowns, designated LS1, LS2, LS3, Figure 1.14.

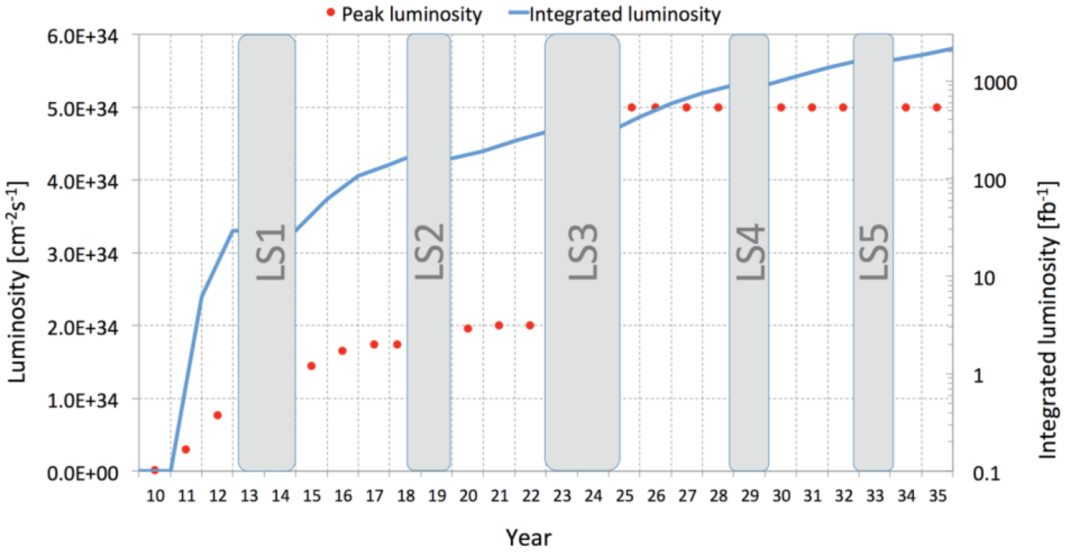

Figure 1.14: LHC performance till 2035. Preliminary dates for long shutdowns and projected luminosities [11].

Run-I covers the period between 2011 and 2012. LS1 started in 2013 and ended in 2015 and modifications were made to the LHC so that a center-of-mass energy of 13 TeV could be achieved. After that the energy would be increased till it reached the desing

energy of 14 TeV.

Run-II from 2015 to 2018 is characterised for the bunch reduction from 50 ns to 25 ns. This change looked for the achievement of the original performance goal for the LHC, which was to operate with 25 ns bunch spacing and an instantaneous luminosity of 1×10^{34} cm^{-2} s^{-1}. During Run-II an average of 25 inelastic interactions per bunch crossing, or pileup (PU), took place at CMS, characteristics for which the detector was designed.

The original luminosity was exceeded before the second long shutdown, LS2. On the LS2 the injector chain is improved in order to emit very bright bunches. Upgrades on CMS were necessary as to maintain its good performance. This program is known as the CMS Phase-I Upgrade.

It is expected for the quadrupoles that focus the beams at the ATLAS and CMS collisions regions to be near the end of their lives as a result of high radiation exposure. The period of the LS3 will be used to change these quadrupoles and replace them with new low-β quadrupole triplets. This change and the addition of crab cavities will optimize the bunch overlap at the interacting region thus increasing significantly the luminosity. The following period with the upgrade LHC is known as the HL-LHC or Phase-II Upgrade. The instantaneous luminosity is proposed to stay at 5×10^{34} cm^{-2} s^{-1} from a potential peak value of 2×10^{35} cm^{-2} s^{-1} at the beginning of fills. This increase in luminosity will rise some challenges that will have to be addressed.

The central program of the HL-LHC will remain the study of the Higgs boson, including precise measurements of the Higgs boson couplings. At the TeV scale the LHC has been working were expected new particle physics could show up, but non of it have been seen in any of the detectors. The reason behind this phenomena could be the existence of this particles at messes above the current level of sensitivity, or their presence at lower masses but with cross section lower than expected. The sensitivity on the search of new particles and new physics increases with the growing luminosity. Examples for the benefits of the high integrated luminosity could be the search for new heavy gauge bosons, to 6 TeV or more, for standard model couplings, or in case for very narrow width resonances, probe regions of 0.5-1 TeV. Similarly searches for extra dimensions, compositeness, leptoquarks etc. can be extended in range by a few TeV. One of the mos remarkable achievements that the LHC could accomplish is the obtainment of evidence of dark matter. If the origin of dark matter is caused by a particle, it definitely does not belong inside our present SM catalogue, and here the finding of supersymmetric particles could mean a considerable progress in the understanding of this subject .

The main challenges that the CMS detector faces with the introduction of the HL-LHC are the radiation damage from the integrated luminosity and the very high pileup from the high instantaneous luminosity:

- **Radiation Damage**: the collision rate at the HL-LHC is expected to be of about 5×10^9 /s. The damage due to the resulting particles from the collision and the radioactivity induced on the material will be substantial leading to a progressive degeneration of the detector performance. This problem becomes noticeable when considering that the total dose of all operations from the start of the LHC till the LS3 is equal to the annual dose the CMS detector will encounter.

  It is found that the biggest source of radiation comes from particle production in proton-proton collisions. Charged particles, mainly pions, produced on the phenomena known as jets, explained previously on Section 1.1, cause ionization while passing through the detectors. They also suffer nuclear interaction producing a cascade of particles that add to the radiation. Photons interact in the material to form e^+e^- pairs or end up in the calorimeter where they interact producing electromagnetic cascades.

  Design of a detector able to withstand the intense radiation maintaining its performance calls for the dose rate and particle fluence for each particle.For this reason, simulations are constantly used to anticipate the magnitude and composition of radiation as a function of luminosity.

  The radiation damage is affects differently each detector and sub-detector. For example, silicon detectors suffers from defects in the silicon lattice which in turn changes the bulk electrical properties of the silicon. On consecuence of this phenomena is that the leakage currents will increase. The full depletion voltage[1] increases demanding for operation with partial depletion which leads to a lower signal. Other example are the calorimeters which are mainly scintillating $PbWO_4$ crystals or plastic scintillating tiles, and their main problem is the loss of transmission. The end result is the drastic decrease in the signal of more than 90%, which also carries a reduction in resolution.

- **High Pileup**: colliding beams are many of intense bunches of protons. The dimensions of the bunch are as follows: length of $\sim$ 5 cm, transverse dimensions of 10 microns and is composed of approximately 10^{11} protons. Separation between bunches is 25 ns, which corresponds to a spatial separation of 750 cm. The collision between two bunches is referred as bunch crossing or BX which happens at a rate of 40 MHz, with 140 interactions per BX. The majority of this interactions are peripheral collisions that do not contribute to the aim of LHC of finding new physics.

  While the number of bunches can not be increased the luminosity at LHC does, resulting in a higher pileup. The increase in the pileup is translated to many more

[1]The voltage required to make the full thickness of the detector depleted from charges, hence making it fully sensitive to a crossing ionizing particle

hits in the tracking detectors, which leads to mismeasured or misidentified tracks. High pileups cause confusion on the trigger and on the offline reconstruction and interpretation of events.

Detector that belong within CMS will need to be upgraded in order to account for this 2 mayor issues that appear with the increased luminosity.

1.3.1 Upgrades of the CMS detector

The Tracker was designed for an average pileup of 50 collisions per bunch crossing. The increase luminosity will present a problem in this area, having on average 140-200 collisions per bunch crossing. This reason leads to the conclusion that a mayor uograde has to take place to keep up with the new HL-LHC.

The radiation damage on this detector is especially important on the pixel sensors which suffer a substantial reduction of the charge collection, and also could lead to a reduction of charge sharing between neighbour pixels resulting in a lose of spatial resolution. Primary vertex reconstruction is directly affected by the decrease of hit-resolution. Other aspect of the high radiation is the damage of the read out electronics, which could cause an important data lose.

New Tracker will need a higher radiation tolerance and an increased granularity in order to maintain its performance after the upgrade. This is achieved by the utilization of planar silicon sensors, divided into small pixels. The detector resolution is less likely to suffer from radiation damage. Other alternative is the use of 3D silicon sensors. They offer a higher radiation resistance due to the fact that the charge collection distance is shorter. One downside of the 3D sensors is the price, making its utilization not viable for large volumes.

The calorimeters run into the same issue as the Tracker, they were not designed to withstand the problems resulting from an increase in luminosity, and this problems become far more noticeable on the endcaps.

The ECAL barrel will benefit from an optimization of electronics, creating a more robust environment against radiation, as well as an improvement of the operating temperature of the system.
The HCAL barrel will have lost light by the final stage of the HL-LHC. This affects the electron and photon identification and reduces the resolution for the reconstruction of neutral hadrons in jets. The proposal for the upgrade is the introduction of a doubly-doped plastic scintillator. Plastic scintillator technology it is found that the primary dopant is sanitized to balance the effects of light production and self-absorption processes. At higher radiation doses, thus more radiation damage, a bigger amount of dopant can result

in a more stable light output, with the issue that this light might be lower.

The endcap calorimeter will be replaced with a high-granularity sampling calorimeter. A new silicon/tunsteng electromagnetic section is incorporated before 2 hadronic sections which use brass as the principal absorber. On the front section it is found, for the active material, silicon. The back section uses plastic scintillator. This desing allows for a great performance in the presence of high levels of pileup.

In the same manner as with the other detectors, changes will have to be introduced to cope with the increase radiation dose. In the case of the muon system, its subdetectors are expected to work properly till the end of the HL-LHC lifetime. The introduced changes on this part of CMS are mainly directed towards the electronics.

Substitution of the electronics become necessary in order to maintain performance on a much harsh environment, as well as provide a more efficient read out as to cope with the higher pileup information.

Chapter 2

MIP Timing Detector (MTD)

The MIP Time Detector (MTD) is a new detector introduced in CMS during the HL-LHC era. The introduction of this detector will bring new functionalities to CMS such as the ability to measure precise time production of minimum ionizing particles (MIP) in order to gain resolution within the approximately 200 almost simultaneous pileup interactions that happen in each bunch crossing. Other functionality added to CMS is the identification of charged hadrons and the fact that it opens the possibility to study new and challenging physics modes as the production of long-lived particles. Main source and further can be found on [12].

The collision rate on the Phase-II Upgrade of LHC will far exceed the previous one, which will demand for significant upgrades to continue its efficient performance. The MTD addition will help CMS to face the challenge of high luminosity. As mentioned on Section 1.3, the peak luminosity expected is 2×10^{35} cm^{-2} s^{-1} and a sable leveled luminosity of 5×10^{34} cm^{-2} s^{-1} limiting the number of interaction to 140 on average. An advanced scenario, with an increase of the leveled luminosity to 7.5×10^{34} cm^{-2} s^{-1} will provide 30% more integrated luminosity producing 200 collisions per BX. Interesting or "hard" interactions to CMS, which are found on the energy scales between a few GeV to the TeV scale, form a 1% of the total BX and will always be accompanied by an average of 140-200 additional collisions. The identification and reconstruction of the hard interactions can be exponentially difficult with the energy deposits and spatial overlap of tracks from the additional collisions which can increase the rate of false triggers. This much harsher radiation and high pileup environment demand for a resistant detector capable of a transport of much higher rate of data for its analysis.

The resolution of the MTD for MIPs will be of 30-40 ps at the beginning of the HL-LHC operation, and it is estimated that it will degrade slowly due to the intense radiation reaching a resolution of 50-60 ps by the end of HL-LHC operations. This resolution allows for the correct assignment of charged tracks to the correct interaction vertices in a BX with an estimated average of 200 collisions. The interaction within a BX do not happen at the same time nor the same place and are distributed in time over an rms of 180-200 ps. The collision vertex can be reconstructed associating tracks from a vertex to hits and the

measured time in the MTD. This way, tracks that seem to point to the vertex but have a different measured time can be eliminated from that particular collision. Association of vertices when vertices are found to be really close together in space is the main benefit of the introduction of MTD, and will provide this functionality on the barrel and the endcap regions up to a pseudorapidity of $\eta \pm 3$.

Introducing the MTD detector on CMS allows for an improvement of the particle-flow performance at high pileup reaching a level of resolution near to the current Phase-I CMS detector, able to handle a pileup of approximately 50. This is observed when considering the beam bunch in pieces of a time exposure of 30-40 ps, finding that the number of interactions for each piece would be of 40-60. In essence, with the increase luminosity, the MTD detector will allow us to recover the Phase-I quality of event reconstruction.

Figure 2.1 shows a simulation of the work of the MTD detector for 200 interaction visully demonstrating its powe of space-time reconstruction and importance.

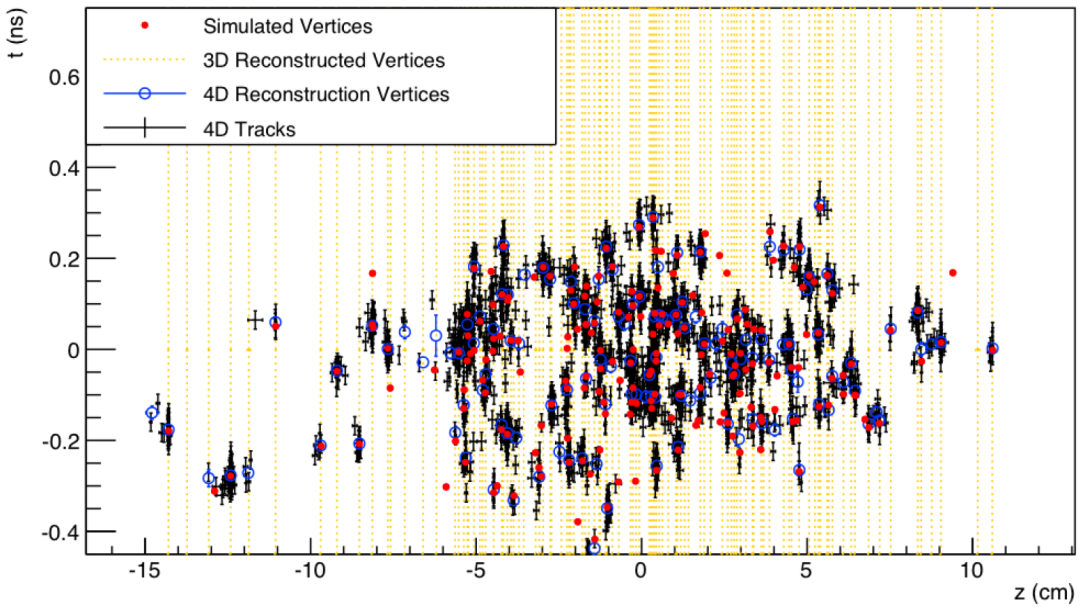

Figure 2.1: Simulation of a 200 pileup assuming a $\sim$ 30 ps MIP timing detector. The horizontal axis gives the position on the barrel with 0 being the point where the beams overlap and the vertical axis displays the time of the event [12].

The reduction of tracks is portrayed on Figure 2.2 with the mean number of wrongly associated tracks to the primary vertex as a function of the line density of the collision vertices. For the peak density for a 200 pileup collision, 1.9 mm^{-1}, without the MTD the number of incorrectly associated tracks reaches over 20.

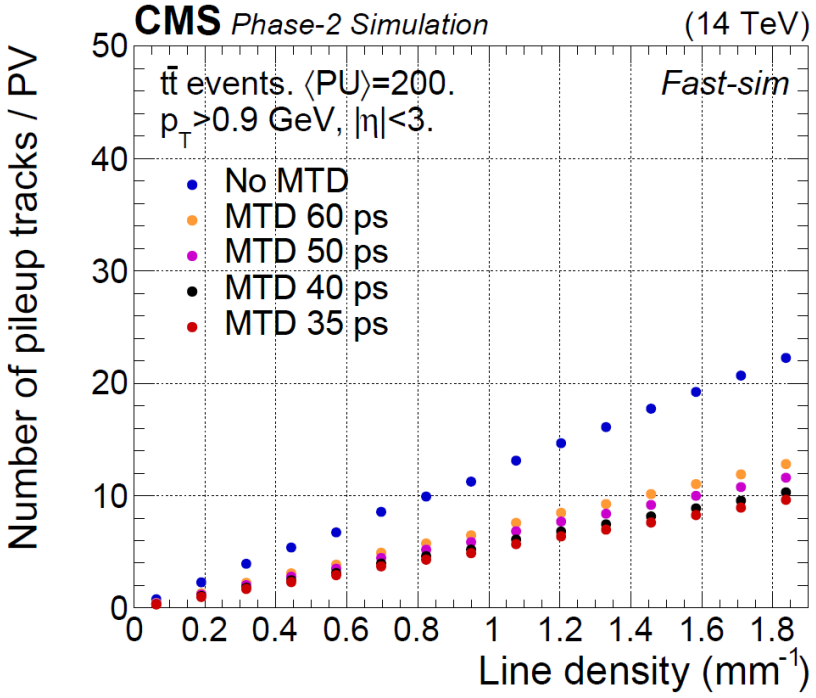

Figure 2.2: Misplaced tracks as a function of the linear density for a 200 interaction pileup, using different MTD resolutions [12].

With the MTD at its peak resolution, 30-40 ps, and a track-time reconstruction efficiency of 85% the wrong associations are reduced by more than a factor of two, which is the same as to lower the peak luminosity from 1.9 mm^{-1} to about 0.8 mm^{-1}, or less than to 80 pileup collisions.

Other benefit of the introduction of the MTD to CMS, apart from preserving the quality of the data, is the possible identification of charged hadrons like pions, kaons, or protons based on the time-of-flight. This result in an enormous step forward on Heavy Ion physics and on specialized QCD studies in pp collisions.

The materials and structure of the MTD are determined by mechanical constraints, radiation tolerance, performance, cost and the upgrade schedule. The MTD will be situated between the Tracker and the calorimeters, divided into Barrel Timing Layer (BTL), which cover the pseudorapidity $|\eta| < 1.5$, and the Endcap Timing Layer (ETL), covering up to $|\eta| = 3$. Here it is found that the radiation environments change drastically for the barrel an the endcaps. For the radius ≈ 1.2 m of the ETL, the dose of radiation received is the same as in the highest $|\eta|$ of the barrel, but at a radius of only ≈ 0.3 m the dose is nearly 30 times higher. Consequences of this behaviour is the utilization of a crystal scintillator with a SiPMs, which are pixelated avalanche photodiodes, in order to read out the signal, on the BTL and for the ETL LGADs, silicon sensors, which give out the best performance.

Due to its lower radiation dose, the BTL uses SiPMs which are not sufficient radiation tolerant to work on the endcap, meanwhile, the LGADs are too expensive to be used on the entirety of the detector. Other reason for the usage of SiPMs on the BTL is the restriction of time on the construction of the barrel thus choosing technology and materials for which its production in industry is well-established. Common systems for both BTL and ETL are the clock and backend systems, cooling and detector slow controls and safety systems.

Layout and configuration of the MTD is shown in Figure 2.3. It is also visible the material used on each part and the characteristics corresponding to the BTL and ETL.

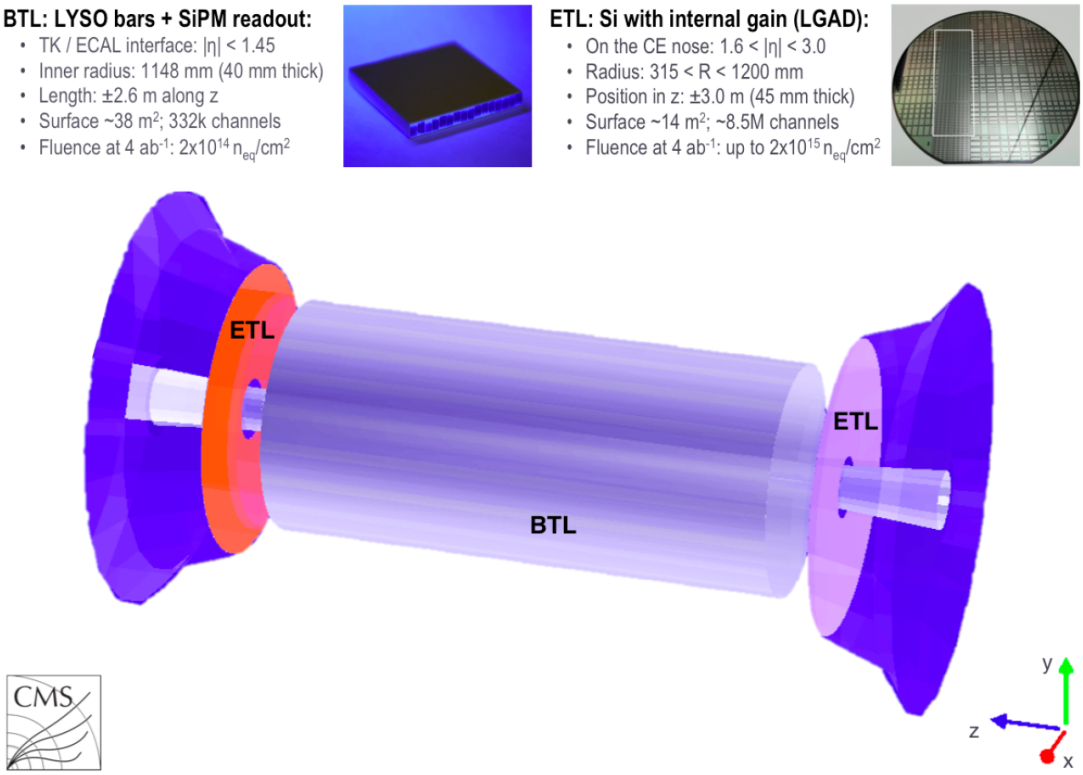

Figure 2.3: Schematic layout of the new detector differentiating the barrel and the two endcaps [12].

From now on, the attention on the MTD detector will be centered on the ETL, being the aim of this project the understanding an utilization of the necessary software and hardware for the construction of the LGADs cells.

2.1 ETL detector

ETL will consist of two disks of MIP-sensitive silicon devices, which will have excellent time resolution, covering a pseudorapidity $1.6 < |\eta| < 3.0$. ETL will be placed 2.98 m from the interaction point. Each ETL counts with two disks populated with sensors on both faces. Sensors are placed on a staggered position as to cover the areas used for read out, power and cable infrastructure on the other face. The MIP sensitive area of each disk is greater than 85%. The utilization of two disks allows for a hermetic coverage with a total sensor area of 7.9 m^2 per endcap, Figure 2.4. Both disks are composed of 4 wedges, which are 4 identical independent 90º structures of detectors, that allows for a better maneuver and access if needed, Figure 2.5.

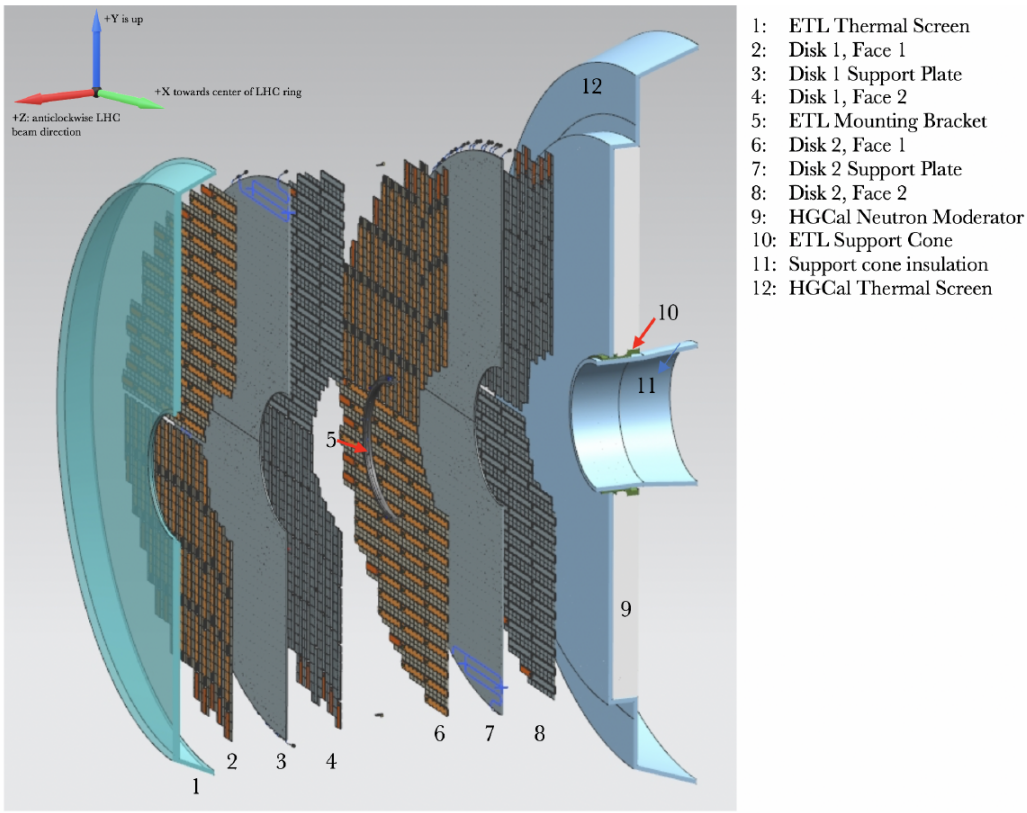

Figure 2.4: Cross-section of the ETL. It is shown the support structures and CO_2 cooling pipe inlets, as well as the 2 detector disks [12].

Placement of the ETL structure will prove to be difficult, as it will be placed between the endcap tracker and the new Phase-2 high granularity endcap calorimeter (CE). The ETL will occupy an independent cold and dry volume in order to facilitate access in case of faulty components. This separation of cooling solutions is also essential as to not interfere with the CE performance. On Figure 2.4 it is also visible the neutron moderator necessary for the correct performance of CE.

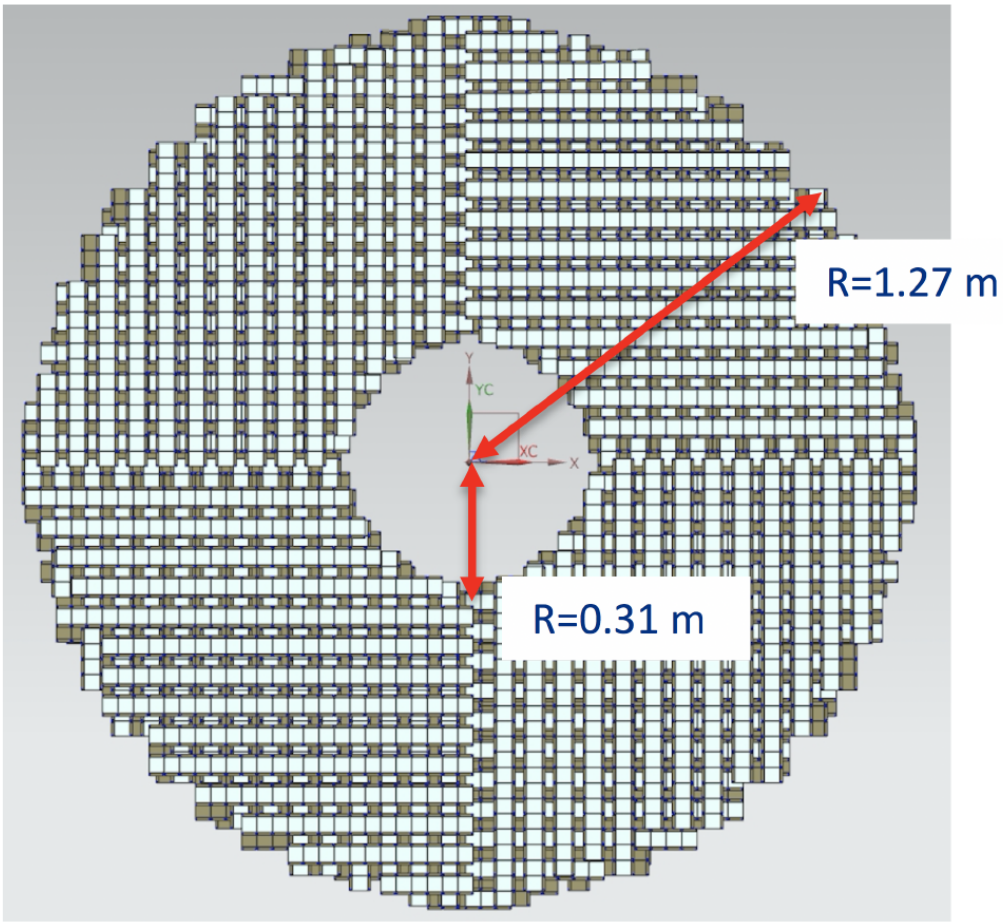

Figure 2.5: Sensor arrangement on one face of a disk [12].

2.1.1 Silicon sensor

MIP timing detector in the CMS will require a uniform and efficient sensor with a high radiation tolerance on the endcap region. It performance must be up to standards till the end of the HL-LHC lifetime. These reasons have lead to the utilization of Ultra-Fast Silicon Detectors (UFSDs), which in essence are planar silicon devices based on the Low-Gain Avalanche Detector (LGAD) technology. This silicon sensors incorporate a low controlled gain in the signal formation mechanism. At electric fields above $E \approx 300$ kV/cm, charged carriers trigger charge multiplication. Electrons, and on a lesser importance holes, have suficient kinetic energy as to generate additional e/h pairs. This electric field is achieved with the appropriate implanted doping density, $N_D \approx 10^{16}$ /cm^3, which locally creates outstandingly high fields when depleted. The gain layer is made by implanting a p-type, avoiding breakdown, with its lateral spread controlled elongating the n-doped portion around it. This portion is called Junction Termination Extension (JTE), Figure 2.6. A clear advantage over the SiPMs is the reduced gain values.

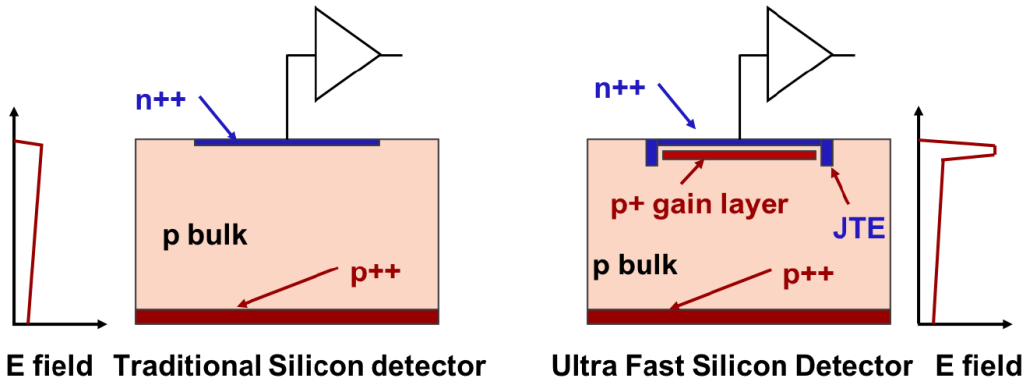

Figure 2.6: Diagram comparing traditional silicon detector and UFSDs [12].

A low gain device requires a size of less than a few mm^2 in order to deliver a good time performance. This leads to the usage of an enormous number of pixels so as to cover the 7.9 m^2 of each ETL. This restrictions fit with the designed sensor, 21.2×42 mm^2 with square pixels of 1.3×1.3 mm^2. The disposition of the sensor on a 15.24 cm or 6-in wafer are shown in Figure 2.7.

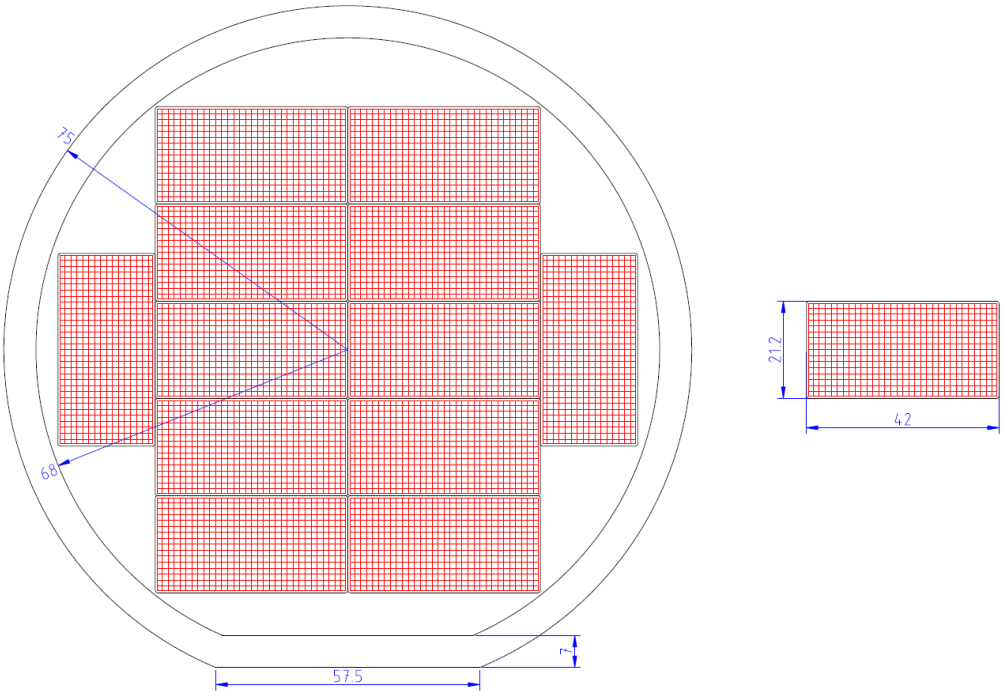

Figure 2.7: Sensor disposition on an 6-inch wafer [12].

Benefits of the use of smaller sensor are as follows: the reduce size of the sensor

makes for a better use of the 6-inch silicon wafers; the smaller sensors have a higher yield.

The usage of silicon carries 3 types of effects due to radiation damage:

1. Decrease of the charge collection efficiency.
2. Increase in the leakage current.
3. Changes in the sensor doping profile.

As it has been made clear, UFSDs are different from standard Pin diodes, thus having this 3 effects different impacts in our sensors. A thinner sensitive region on the UFSDs makes for a moderate decrease of the charge collection efficiency due to radiation. THe same reason leads to a moderate increase in the leakage current. Leakage current ought to be kept low in order to guarantee low power consumption and a low shot noise. The mayor impact to the gain mechanism and performance of the detector comes from the changes on the sensor profile.

2.1.2 ETL modules

The ETL modules are built from sub-assemblies, which facilitates the robot work, containing a sensor and 2 ETROCs. The ETROC are the ETL readout ASIC[1] chips. ETROCs are designed for them to handle a 16×16 pixel cell matrix. Each pixel will have a size of 1.3×1.3 mm^2 therefore matching the LGAD sensor pixel size.

The final built and assembled ETL module is shown in Figure 2.8, as wll as a deconstructed view showing each of the parts. The normal configuration of the modules would be the one displayed on Figure 2.8 (left) with the single module, Figure 2.8 (right), placed on the edges of the cooling disk in order to increase the coverage in this areas. If we take the norma configuration as double module the number of ETROCs also increases to 4.

Modules are glued to an Aluminum Nitride (AlN) substrate which serves as a baseplate. AlN has a thermal expansion coefficient similar to that of the silicon, and also provides a cooling path. On the matter of cooling, on the other side of the AlN baseplate a conductive film is glued. It is important for the other side of the conducting film not to be sticky so that replacement of modules becomes possible. As seen in Figure 2.8, the green flexed circuits will be placed on each side of the AlN baseplate. The bias voltage necessary for the correct performance of the detector is provided by the flex circuit, going from the pads on the end of the circuit to the top of the sensor. An AlN cover is placed atop the structure with the function of protecting the sensor.

[1] An application-specific integrated circuit.

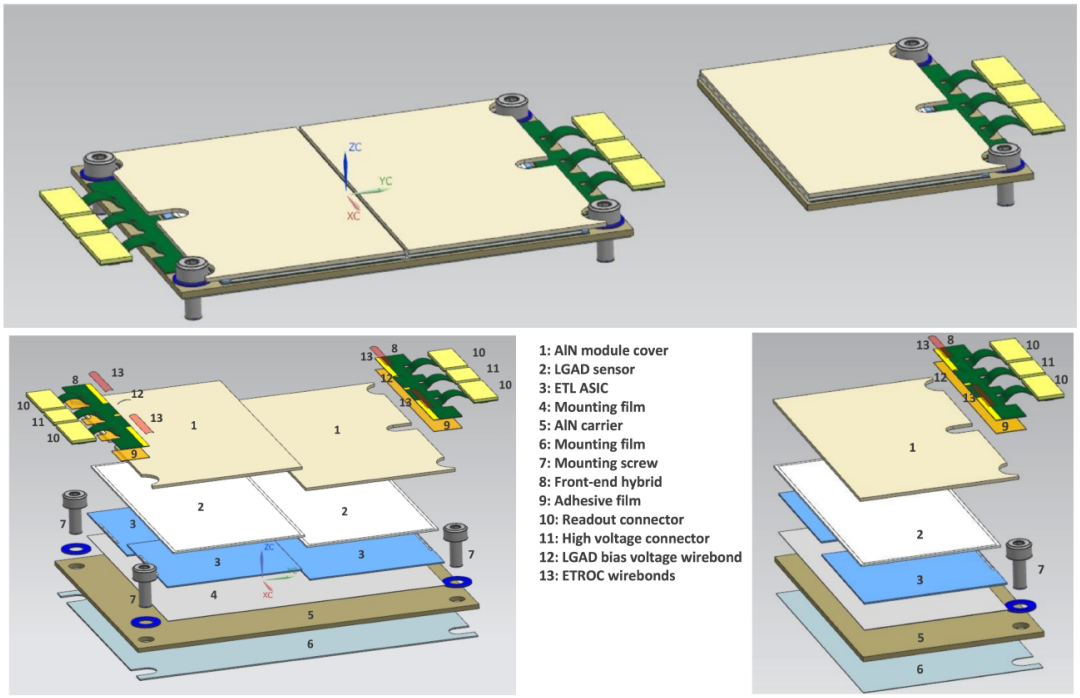

Figure 2.8: Assembled modules (top), details of each module (bottom) [12].

Chapter 3

Robot programming

The final goal this project is the amortization of the building process of the ETL modules described on subsection 2.1.2. The assembly of this modules will be carried out simultaneously by Fermilab, Nebraska's university, the INFN and the IFCA. Roughly 9000 modules have to be built, making the amortization the only way of achieving its construction before the deadline. The objective of the work done on this part of the project is to test the capabilities and performance of the robot, to see if it is up to this challenging task.

Figure 3.1: Robot owned of IFCA. Adept Python linear modules.

The routines created during the project were destined to be used on the Adept Python Linear Modules robot owned by IFCA on the University of Cantabria, Figure 3.1. Due to

external circumstances, the the work has been limited to a simulated environment, relying on a different robot model. This inconvenient do not cause a mayor problem due to the compatibility of the code between the two robots.

The programming language used during the project has been V+. This decision was forced on us when the robot choosing decision was made, as the only language which allows the usage of this robot is V+. Is a high level, event oriented language. As a simulation exercise, visualization of the robot was necessary, and for this reason, ACE 4.0 software was chosen for the project, Figure 3.2.

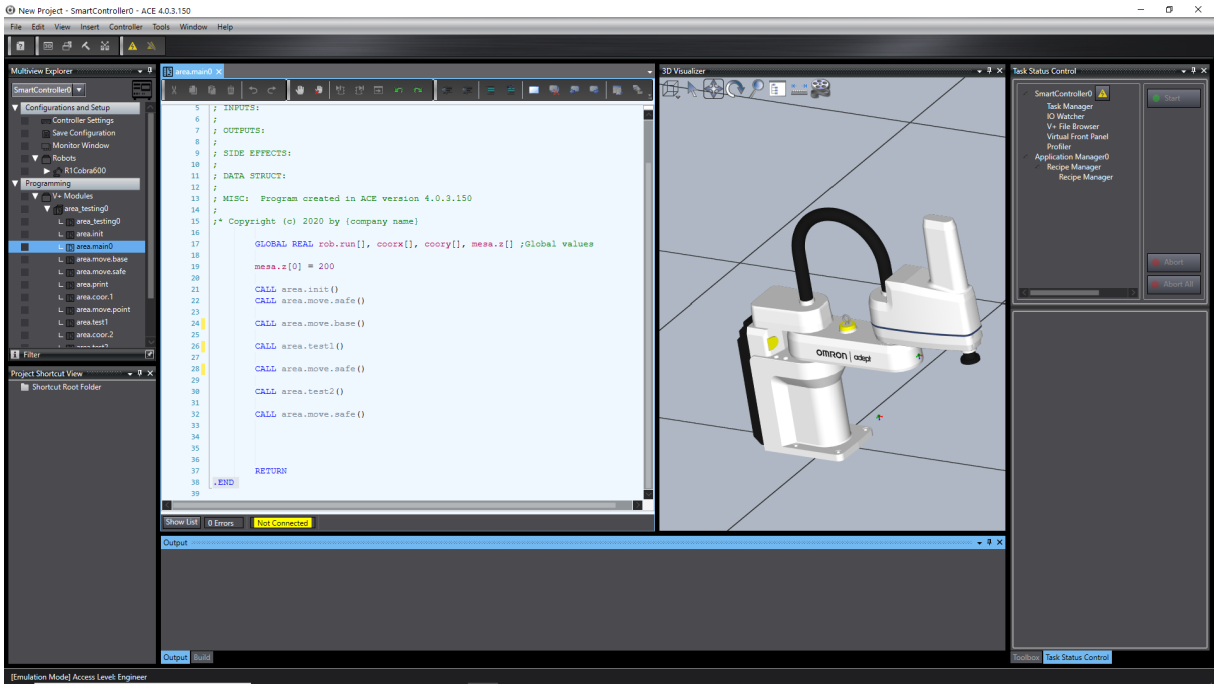

Figure 3.2: Chosen software, ACE 4.0, for the project.

The provided robots on the used software did not include the Adept Python Linear Module. A selection of a robot that could meet the required capabilities thus allowing interchangeable code was necessary. Final selection was the Adept Cobra 600 (lite), which provides a range of motion equivalent to that of the original robot. It counts with a fixed stand, two joints, that allow movement on the $x-y$ plane and a tool holder with it range of motion limited to the z axis, Figure 3.3.

Early stages of the project for the construction of the ETL modules require the testing of the hardware and software used for its assembly. A test of the velocity and precision of the robot as well as a test of the range of motion necessary for the assembly of the module, therefore two test were implemented: a precision and velocity test, and an assembly test.

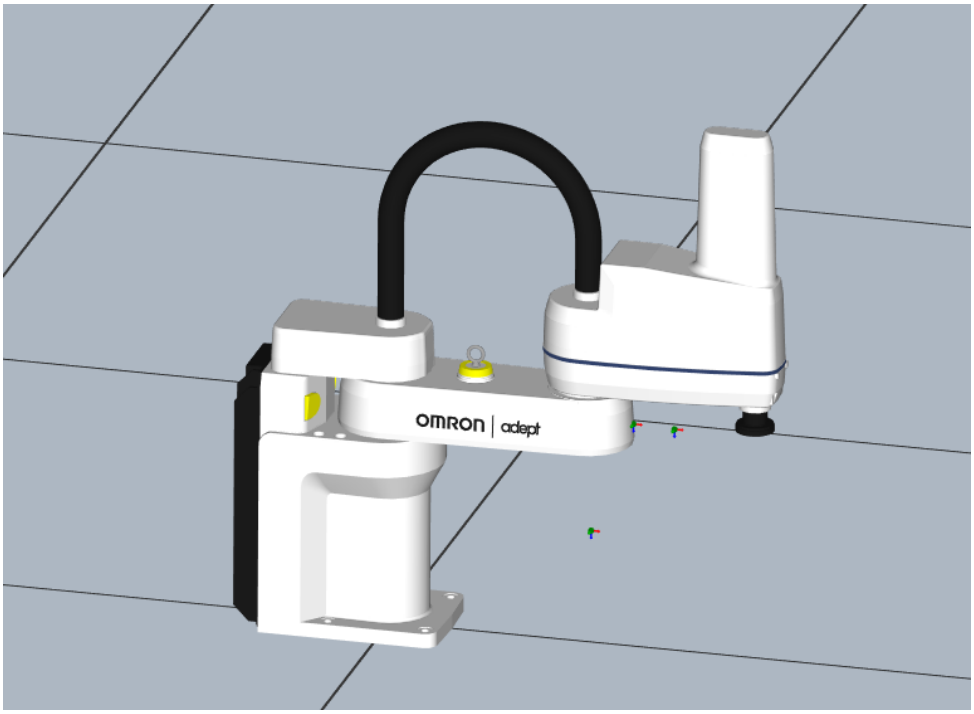

Figure 3.3: Adept Cobra 600 (lite). Chosen robot for the simulation exercises.

3.1 Velocity and precision test

The assembly of the modules is a task that requires an enormous precision due to the size and the fragility of the components. The code integrated for this test has to allow for optimize movement between the chosen points. The general motion trying to be achieved is to reach the testing point from above and leave the same way. This motion allows for a clear movement avoiding obstacles through the procedure.

A layout for the velocity and precision test is shown in Figure 3.4. The aim of the test is to reach every point in display. Initial approach to the problem calls for the creation of a program that would allow movement between points including the described vertical motion on the z axis, thus simplifying the problem. The real world specifies certain condition such as the existence of a table or surface to work in, and for that reason, a height for the table was established as fix value. Once this parameters and the initial code was established, the final step is the correlation of the position of each point to coordinates of the system established on the software.

Simulation does not allow for a precision nor velocity test. The experiment designed for such a task would ask for the creation of a sensor that would have the characteristics of Figure 3.4, and a laser attached to the en of the tool handling arm of the robot. once the code is executed, the sensor would allow for the measurement of the position while the velocity will be taken from the spent in completing the hole test.

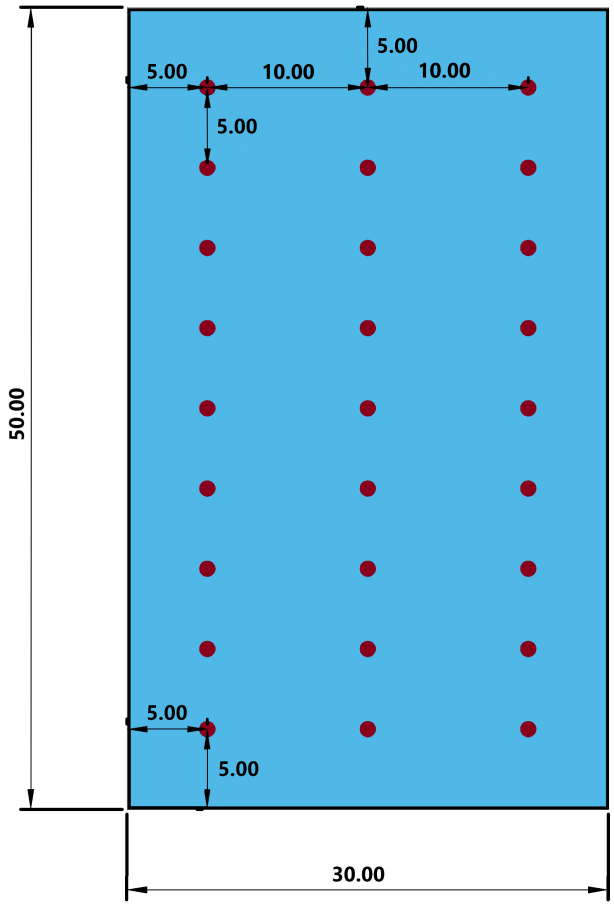

Figure 3.4: Layout of points for the velocity and precision test. Distances given in centimeters.

The simulation gives out information of the operation of the robot. The joint of the robot create a liability when the points are near its body. This causes for the robot to decelerate on this points. This problem is totally bypassed when the Adept Python Linear modules are used due to the absence of joints.

3.2 Assembly test

The assembly test consists on the simulation of an assembly environment in order to check if the range of motion of the robot allows for the completion of a successful run.

This test shares some characteristics with the previous test, such as the need for a vertical movement along the z axis at the beginning of each movement on the $x-y$ plane. The table is set at the same height and its dimensions remain the same.

The layout used on the second test is shown in Figure 3.5. Components of the Figure have been mentioned on subsection 2.1.2. The grey pads are the LGAD sensors, the yellow and black pads are the AlN covers and baseplates, the blue square pads are the ETROCs and the purple pad is the adhesive dispenser.

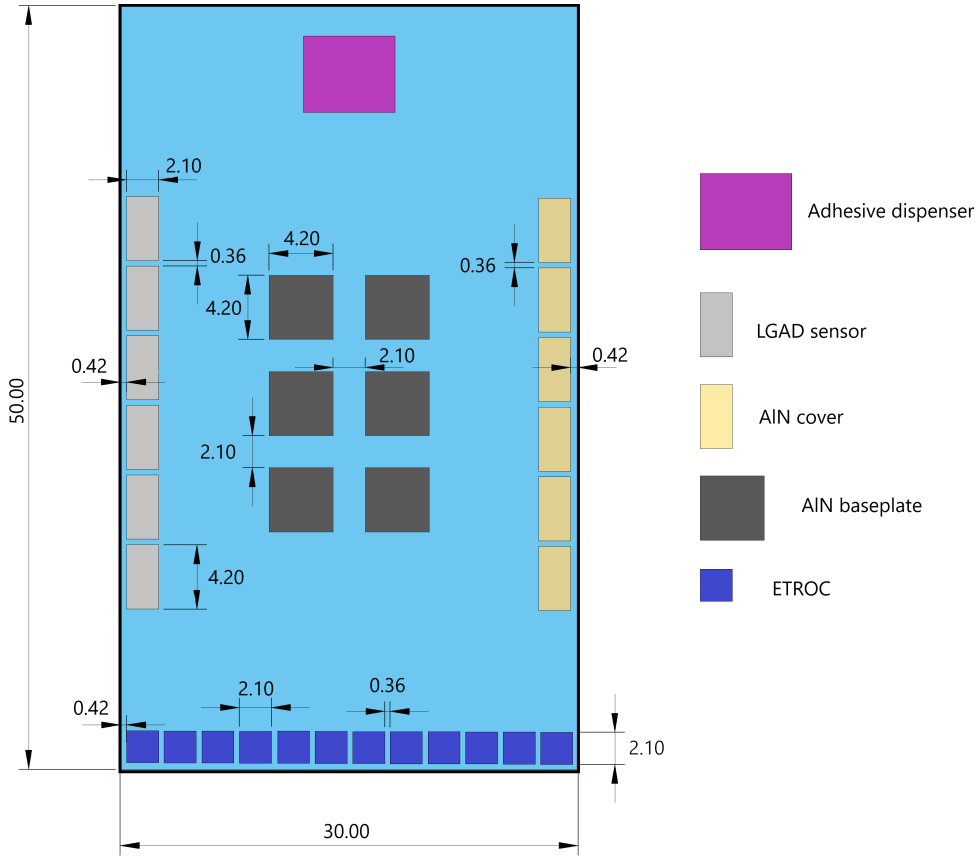

Figure 3.5: Layout of the components for the assembly test: the gray rectangles represent the sensors, the yellow are the AlN covers while the black are the AlN baseplates, the blue squares are the ETROCs, and finally the purple figure is the adhesive dispenser. Distances given in centimeters.

The test starts with the selection and pick up of an ETROC. This ETROC is taken to the adhesive dispenser where the adhesive is applied to finally be place on one of the AlN baseplates. This procedure will be done 3 times more so that the module has 4 ETROCs. This ETROCs will be place in such a manner that the surface of the baseplate is completely covered. The order in which the ETROCs are piked up is always from left to right. The next movement is the selection of an LGAD sensor which will be place on top of the ETROCs previously place. In the same way as in the ETROCs pick up, the sensor is taken to the adhesive dispenser before being place in the module. The sensor pick up is done twice, so each module has 2 sensors. Finally, the AlN covers are selected and in the same way as in the previous step, 2 covers are picked and placed on the module. the

order for both the LGAD sensors and the AlN covers is from top to bottom.

The movement of the robot while is transporting the pieces always stays 10 cm above the table in order to avoid any collision with other elements. The Figure 3.5 shows 12 ETROCs, 6 LGAD sensors and 6 AlN covers. The number of elements only allows for the construction of 3 modules, using 3 AlN baseplates. This means that in the middle of the program, the ETROCs, LGADs and AlN covers have to be restocked.

Chapter 4

Conclusions

The installation of the ETL modules within the LHC structure will hopefully bring about a new era of particle physics discovery, expanding in this way our knowledge about the universe. Operation of the HL-LHC will present enormous challenges without the introduction of the MTD. The incoming information about the pileup will be unmanageable and reconstruction of some collision vertices will become impossible. Other essential aspect that makes the construction of this modules imperative is the high resistance to radiation that its barrel counterpart do not posses.

As mentioned before on chapter 3, the assembly of the modules will be carried out by different institutions, Fermilab, Nebraska's university, the INFN and the IFCA, which in total will have to build roughly 9000 modules, requiring the amortization of the process.

The construction of the modules is feasible with the technology and tools described on chapter 3. The V+ language is not very well established or spaded in the community, and for that reason the only learning process comes from the language guide. However, its use is very intuitive and easy, provided that it is a high level programming language desing exclusively for robot programming.

Characterising the robot, and establishing its capabilities is the initial step on this project, which ends with the construction of the ETL modules. This reason have lead to the creation of this tests. The first test allows for the measurement of the velocity of the robot as well as the precision, 2 essential features for the construction of the modules. The second test creates an assembly environment giving a sense of the range of motion needed for the manufacture of the modules.

Information about the robot performance on the real world becomes a matter of executing the desing code, due to the compatibility of the robots, and the sufficient characteristics of the Adept Python Linear modules. Future work will require a more advanced assembly set up as well as new code in order to allow new action such as the adhesive distribution on the parts that form the module.

Code developed during the project is available here [13].

Bibliography

[1] M. Thomson, *Modern particle physics*. Cambridge University Press, 2013.

[2] B. R. Martin and G. Shaw, *Nuclear and particle physics: an introduction*. John Wiley & Sons, 2019.

[3] urlhttps://home.cern/science/physics/z-boson.

[4] L. Evans and P. Bryant, "LHC machine," *Journal of Instrumentation*, vol. 3, pp. S08001–S08001, aug 2008.

[5] L. Evans and P. Bryant, "LHC machine," *Journal of Instrumentation*, vol. 3, pp. S08001–S08001, aug 2008.

[6] urlhttp://cds.cern.ch/record/841568/files/lhc-pho-1993-008.jpg?version=1.

[7] urlhttp://cds.cern.ch/record/2725741/files/?ln=es.

[8] urlhttps://www.oeaw.ac.at/en/hephy/research/cms-experiment-at-lhc/.

[9] urlhttp://cdsweb.cern.ch/record/1178706.

[10] urlhttps://home.cern/resources/image/experiments/alice-images-gallery.

[11] C. Collaboration *et al.*, "Technical proposal for the phase-ii upgrade of the compact muon solenoid, cms technical proposal cernlhcc-2015-010," tech. rep., CMS-TDR-15-02, CERN, 2015. https://cds. cern. ch/record/2020886, 2015.

[12] C. Collaboration, "Technical proposal for a mip timing detector in the cms experiment phase 2 upgrade," tech. rep., 2017.

[13] urlhttps://github.com/VictorCalzada/Robot-software-for-the-assembly-of-modules-of-the-Endcap-Timing-Layer-of-the-CMS-detector.